remote sensing

MDPI

Technical Note

Study on the Source of Debris Flow in the Northern Scenic Spot of Changbai Mountain Based on Multi-Source Data

Jiahao Yan [1], Yichen Zhang [1,*], Jiquan Zhang [2], Yanan Chen [1] and Zhen Zhang [1]

[1] School of Jilin Emergency Management, Changchun Institute of Technology, Changchun 130021, China
[2] School of Environment, Northeast Normal University, Changchun 130024, China
* Correspondence: zhangyc@ccit.edu.cn; Tel.: +86-1384-402-8326

Abstract: The northern scenic area of Changbai Mountain is a high-incidence area of debris flow disasters, which seriously threaten the safety of tourist's lives and property. Monitoring debris flow and providing early warning is critical for timely avoidance. Monitoring the change of debris flow source is an effective way to predict debris flow, and the change of source can be reflected in the settlement deformation of the study area. The offset tracking technique (OT) is insensitive to the coherence of SAR images and can resist the decoherence of D-InSAR and SBSA-InSAR to a certain extent. It is a technical means for monitoring large gradient deformation. It has been widely used in the field of seismic activity, glaciers and landslides in recent years, but few scholars have applied this technique in the field of debris flow. In this paper, we use OT techniques in combination with field surveys, Google imagery and Sentinel-1 data to monitor surface deformation in the northern scenic area of Changbai Mountain in 2017 and use D-InSAR techniques to compare and complement the OT monitoring results. The results of this study show that for monitoring surface deformation in the study area after a mudslide, it is better to use both methods to determine the surface deformation in the study area rather than one, and that both methods have their own advantages and disadvantages and yet can complement each other. Finally, we have predicted the development trend of mudflows in the study area by combining the calculated single mudflow solids washout, which will help to improve the long-term monitoring and warning capability of mudflows in the study area. The study also enriches the application of offset-tracking technology and D-InSAR in the field of geohazard monitoring and provides new ideas and methods for the study of mudflow material source changes.

Keywords: Changbai Mountain North Scenic Area; debris flow source; D-InSAR; offset-tracking; surface deformation

Citation: Yan, J.; Zhang, Y.; Zhang, J.; Chen, Y.; Zhang, Z. Study on the Source of Debris Flow in the Northern Scenic Spot of Changbai Mountain Based on Multi-Source Data. *Remote Sens.* **2023**, *15*, 2473. https://doi.org/10.3390/rs15092473

Academic Editors: Stefano Morelli, Veronica Pazzi and Mirko Francioni

Received: 14 March 2023
Revised: 20 April 2023
Accepted: 4 May 2023
Published: 8 May 2023

1. Introduction

Debris flow is a sudden geological disaster that occurs in mountainous or ditch areas [1–4], widely distributed in some areas of the world with special topography or geomorphology [5–9]. Debris flows are very destructive [10–14]; they can rush out a large amount of material sources in a short time, which even include huge rocks, which will pose a great threat and damage to the ecological environment, life, property and construction facilities in the basin [15–19]. Therefore, how to monitor and warn debris flow is the focus of current research, and it is also a key problem that needs to be solved urgently.

The formation of debris flows needs to meet three conditions: steep terrain, sufficient rainfall and rich debris flow source. The total quantity of material sources determines the occurrence of debris flow and its degree of risk. The greater the reserves of material sources, the greater the risk of debris flow. It is necessary to know the quantity of material sources in the source area of debris flow to accurately evaluate the hazards of debris flow in the basin [20,21].

Changbai Mountain is an area which is highly prone to geological disasters. It has a main debris flow ditch and eight branch ditches. Almost every year, disasters of different

scales occur, which seriously threaten the safety of tourists' lives and property. In order to better carry out geological disaster warnings in time, it is urgent to carry out the professional monitoring of important hidden danger points of geological disaster in order to minimize the possible losses caused by such disasters. In recent years, with the rapid development of observation technology, scholars have used different technologies to obtain the provenance of the study area. For example, aerial photos taken from aircraft or drones [22], satellite images [23] and aerial laser scanning [24]. However, if we also adopt the same method to evaluate the source of debris flow in the northern scenic spot of Changbai Mountain, it is not enough for us to dynamically monitor the debris flow in the dangerous area; because we do not know the source of the change in the source area after a debris flow occurs, using the same method to assess the source will be very cumbersome and time-consuming [25–29]. Therefore, the deformation monitoring of debris-flow-dangerous areas is of great significance to the early warning of debris flow. The main observation method of traditional settlement observation technology is to use a total station, a level and other equipment to lay a certain number of monitoring points on the ground for continuous observation, and then to invert the surface deformation of the whole study area according to the deformation of the monitoring points, which belongs to the single-point measurement method. This method cannot reflect the deformation state of the whole study area and has great limitations [30,31].

Previous studies have mostly applied offset-tracking technology to the fields of earthquakes, glaciers and landslides, but few people have applied this technology to the surface deformation monitoring of debris flows [32–36]. Chen used SBAS-InSAR technology to monitor the deformation of the debris flow source area of Xulong Ditch and obtain the annual deformation of the area [20]. However, the premise of their application of this method is that there is no debris flow or landslide in the study area, and the annual settlement is very small. Once a large area of deformation occurs due to natural disasters in this area, the method will fail. In addition, in areas with complex terrain, some noise information will be added in the image processing process, and some accuracy will be lost in small-scale monitoring; hence, it is easy to form unreliable monitoring results. Therefore, the accuracy of offset tracking (OT) is not high enough, but it is a powerful tool when other methods fail.

In this study, first, we conducted a field survey of the study area and calculated the storage of loose solid matter sources in the study area; the second step calculated the quantity of solid matter sources flushed out of each debris flow ditch in the study area in 2017; in the third step, we used offset tracking to monitor the deformation of the research area, and we obtained the deformation of the research area in each season; in the fourth step, D-InSAR was used to monitor the deformation of the research area, although decoherence will occur in severely deformed areas, but it can be used as a supplement to the offset-tracking technology in the slow-deformation area to obtain higher-precision deformation values. Combining remote sensing images and field surveys, the debris flow danger zone was delineated, and the development of debris flows was predicted based on the surface deformation of each debris flow ditch combined with the calculated amount of debris flow solids. These research results will help to improve the long-term monitoring and of mudslides in the study area and, with improved early-warning capabilities, further protect people's lives and properties. The research also enriches the application of offset-tracking technology and D-InSAR in the field of geohazard monitoring and provides new ideas and methods for the study of mudflow material source changes.

2. Study Area

Changbai Mountain North Scenic Area is located in the southeast mountainous area of Jilin Province, China, with the geographic coordinates of 127°28′–128°16′E and 41°42′–42°25′N. It belongs to the humid area of the mid-latitude continental monsoon climate. The climate is characterized by long and cold winters and warm and short summers. Affected by the terrain and the continental and Pacific air flow, the vertical zoning is obvious, and the temperature and rainfall are controlled by altitude. According to the

relevant data, the terrain increased by 100 m, the temperature decreased by 0.5~0.6 °C and precipitation increased by 30 mm. The average annual precipitation is 1407.6 mm, and the precipitation is concentrated in June and August. The precipitation in three months accounts for more than 60% of the total annual precipitation, and most of it results from rainstorms. The highest peak in the study area is Tianwen Peak, which is located in the northeast of Tianchi and has an altitude of 2670 m. The peak is composed of gray and pale white pumice and is opposite Longmen Peak, forming a "U"-type valley between them. From south to north, Changbai Mountain's waterfall forms the source of the two white rivers. The main types of geomorphological genesis in the study area are eroded volcanic terrain and tectonic erosion terrain. The two sides of the "U"-shaped valley are formed by volcanic cones and their extended mountains, and the canyon area is a ditch formed by the Erdaobai River fault. Figure 1 is distribution of disaster sites in study area.

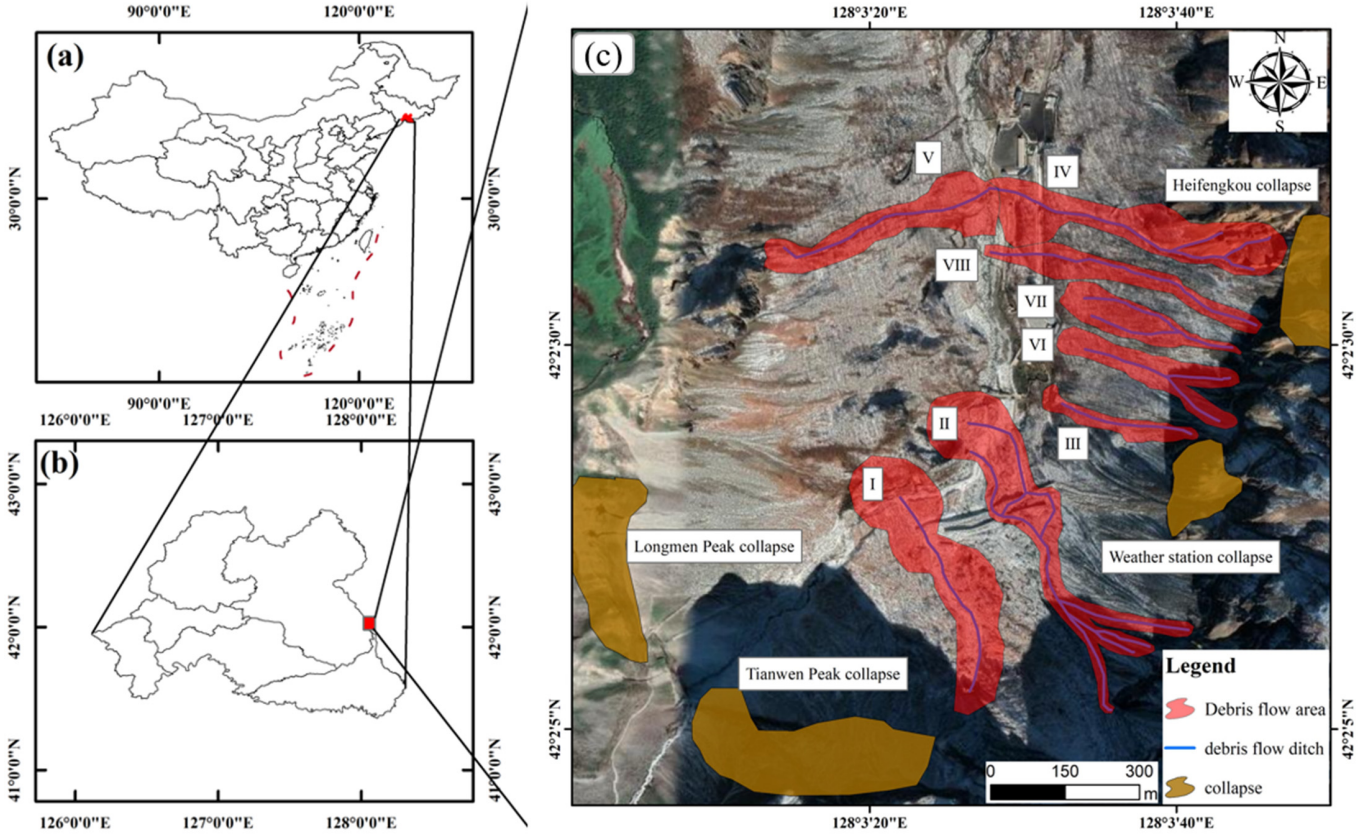

Figure 1. Distribution of disaster sites in study area. (**a**) Location of the study area in China; (**b**) location of the study area in Baishan City; (**c**) extent of debris flow and location of the collapse in the study area.

There are eight debris flows along the Erdaobai River in the northern scenic area of Changbai Mountain (Table 1). The Erdaobai River is generally a deep-cutting "U"-type valley, which has the characteristics of a steep slope and a large cutting depth. The longitudinal length of the main ditch is 9.1 km, and the average longitudinal slope of the main ditch is 48‰. Among them, the longitudinal slope of the upper reaches from the Tianchi waterfall to the intersection of the No. 6 branch ditch is steep, with an average longitudinal slope of 237‰, and the middle part of the Guanyatai section is slightly slow, with an average longitudinal slope of 105‰. In the lower reaches of the main ditch, the longitudinal slope is slightly slow, with a longitudinal slope of 51‰, and it shows obvious spatial variation characteristics of steep up and slow down.

Table 1. Statistical table of basic characteristics of each debris flow tributary ditches of Erdaobai River.

The Serial Number	Ditch Length (km)	Ditch Area (km^2)	Relative Elevation Difference (m)	Mean Longitudinal Slope (‰)
1	1.53	0.48	618	403
2	1.45	0.46	664	458
3	0.76	0.10	434	569
4	0.80	0.10	356	446
5	0.79	0.08	390	466
6	0.82	0.09	429	522
7	0.80	0.07	392	487
8	0.84	0.08	393	468

The eight tributaries in the study area are not composed of typical formation areas, formation circulation areas and accumulation areas. Therefore, according to the formation conditions and movement mechanism of debris flow and the distribution of loose solid sources of debris flow, the ditch area is divided into three areas: the catchment area in the upper reaches of the ditch, the formation circulation section in the middle reaches and the circulation accumulation area at the intersection of the ditch mouth to the Erdaobai River. The No. 1 ditch has the largest ditch area. Taking the No. 1 ditch as an example, Figure 2 is the GIS interpretation map of three sections of the No. 1 ditch, and Figure 3 is the cross section of the No. 1 ditch.

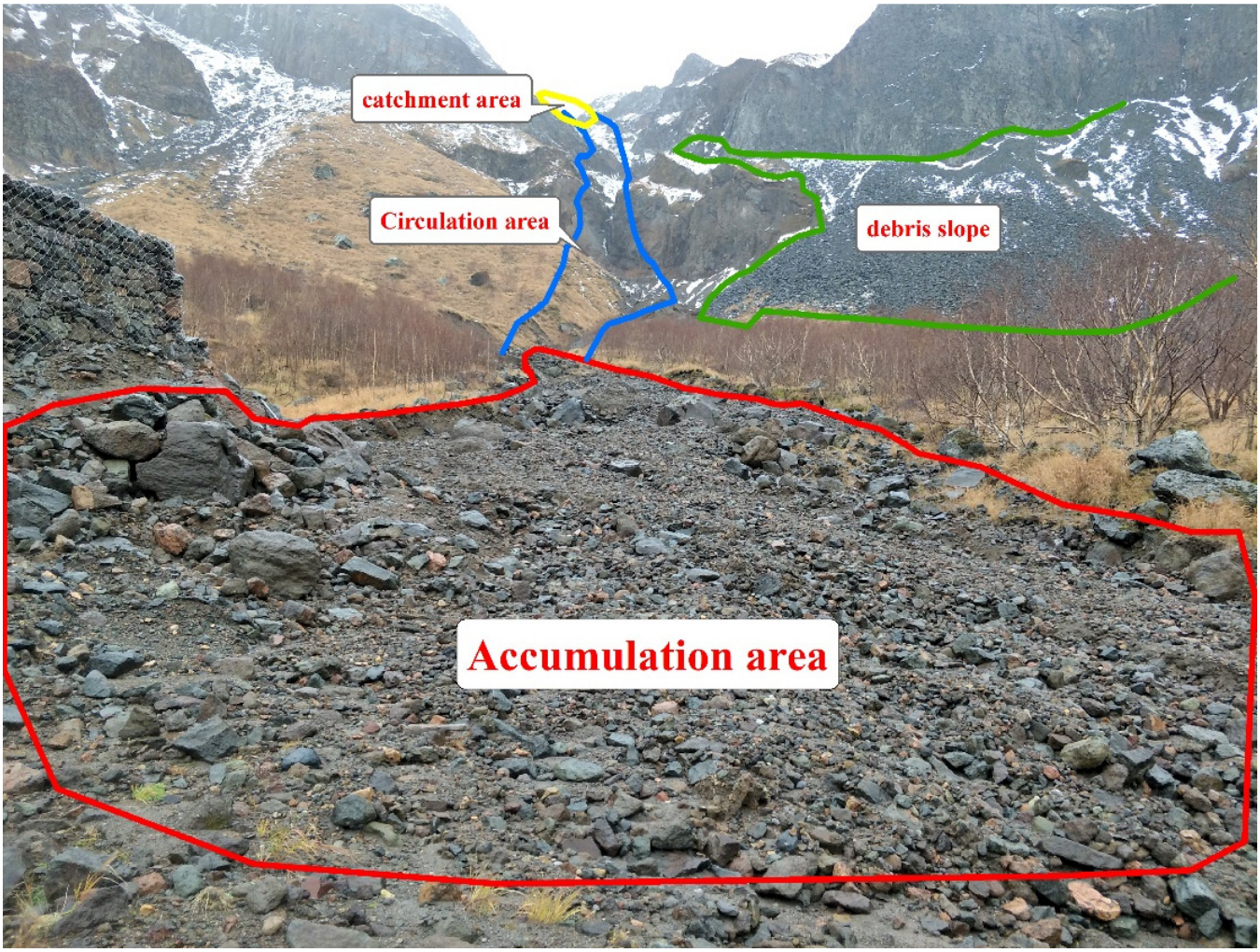

Figure 2. No. 1 debris flow ditch, three sections.

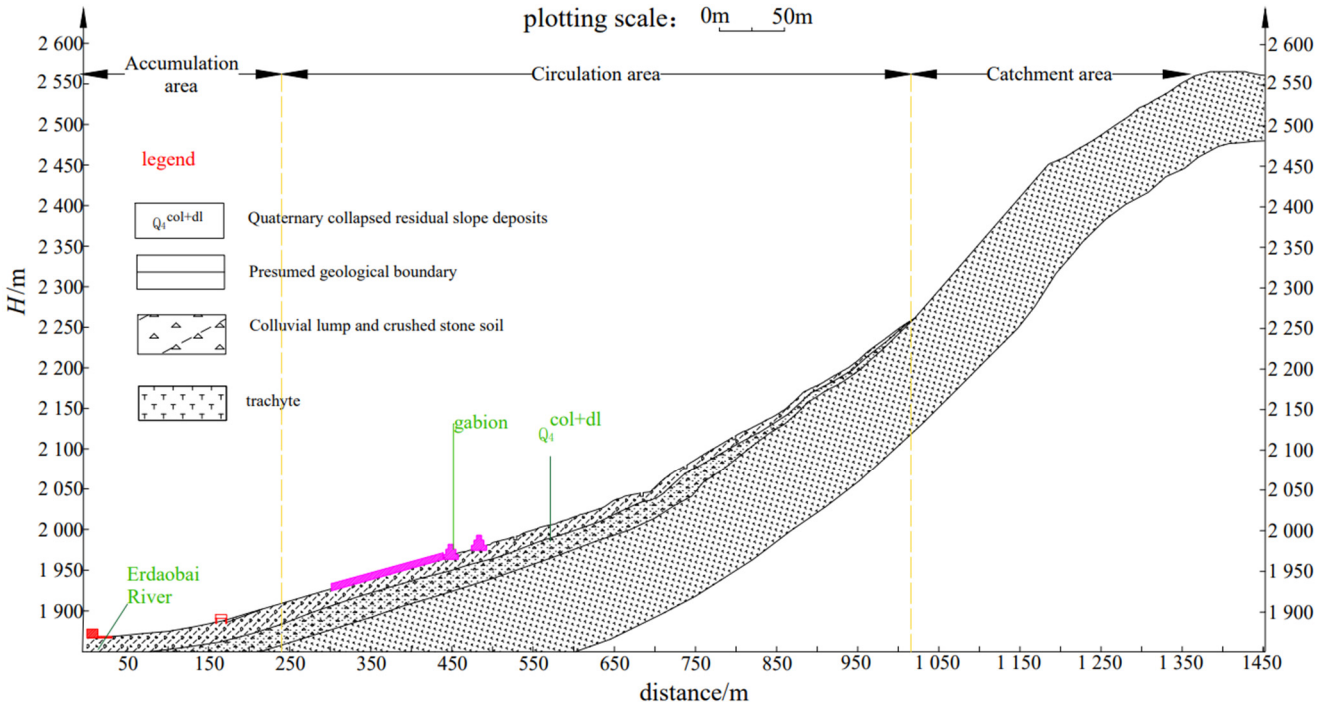

Figure 3. No. 1 debris flow ditch sectional drawing.

3. Data and Methods

3.1. Field Investigation

From 6 September 2018 to 15 October 2018, project team members conducted a 40-day on-site geological survey of the North Changbai Mountain Scenic Area. The topography and geomorphology of the working area, the environmental geological problems in the area, the development history, the genetic mechanism and stability of the deformation and the failure of the hidden danger points of geological disasters were investigated. In addition, geophysical exploration work is carried out by the high density resistivity method in the debris flow formation and accumulation area. The geophysical prospecting in the accumulation area mainly elucidates the thickness, erosion and deposition amplitude, distribution range and lithology composition of the debris flow accumulation fan, which lays the foundation for finding out the formation conditions and characteristics of the debris flow. The geophysical exploration of the formation area needs to elucidate the source reserves. The source types mainly include the following: landslide accumulation source, slope erosion source and ditch accumulation source.

3.2. Calculation of Solid Discharge of Debris Flow

On 2 July 2017, a heavy rainfall with an hourly rainfall intensity of 22.4 mm·h^{-1} in the northern scenic spot of Changbai Mountain triggered debris flows in 8 branch ditches. The relationship between the loose source, basin shape and debris flow discharge can be analyzed by calculating the single debris flow solid discharge. At the same time, the maximum amount of debris flow is an important parameter in the design of a debris flow disaster prevention and mitigation project, which can provide a scientific basis for debris flow disaster prevention and control. The single debris flow solid ejecta is calculated according to the calculation formula provided of the "Debris Flow Disaster Prevention Engineering Exploration Specification" (DT/T0220-2006),

$$Q_H = Q(\gamma_c - \gamma_w)/(\gamma_H - \gamma_w) \quad (1)$$

where Q_H—total amount of solids washed out by debris flow (m^3); Q—total amount of debris flow (m^3); γ_c—debris flow severity (t/m^3); γ_w—water severity (t/m^3); and γ_H—solid material weight of debris flow (t/m^3).

The total amount of debris flow in one time, Q, is calculated according to the formula provided of the Code for Exploration of Debris Flow Disaster Prevention Engineering (DT/T0220-2006):

$$Q = KTQ_c. \quad (2)$$

In the formula, T—debris flow duration (s); and Q_c—debris flow maximum flow (m/s).

Through inquiry with the supervision staff of the scenic spot, it became known that the debris flow lasted for 900 s except for ditches No. 3 and No. 8, for which is lasted about 15 min, and the debris flow in the remaining trenches lasted 10 min (600 s). The values of K are shown in Table 2:

Table 2. K value reference table.

Catchment Area *F*	Value of *K*
$F < 5$ km^2	$K = 0.202$
$F = 5$~10 km^2	$K = 0.113$
$F = 10$~100 km^2	$K = 0.0378$
$F > 10$~100 km^2	$K < 0.0252$

The peak flow of debris flow, Q_c, is calculated according to the calculation formula provided of 'Debris Flow Disaster Prevention Engineering Exploration Specification' (DT/T0220-2006):

$$Q_c = (1 + \phi)Q_p D_c, \quad (3)$$

where Q_c—debris flow section peak flow (m^3/s); ϕ—sediment correction factor, determined by look-up table method as $\phi = 0.88$; Q_p—rainstorm peak discharge; and D_c—blockage coefficient, determined as $D_c = 1.8$ according to survey specification Table 1.

Q_p calculated the surface water catchment flow according to the empirical formula proposed by China Institute of Highway Science:

When the catchment area $F \geq 3$ km^2, the formula is

$$Q_p = \psi F^{\frac{2}{3}} S. \quad (4)$$

When the catchment area $F < 3$ km^2, the formula is

$$Q_p = \psi F S, \quad (5)$$

where Q_p—storm flood peak discharge (m^3/s); ψ—rainstorm runoff coefficient; F—catchment area (km^2); and S—hourly rain intensity (mm/h).

3.3. Offset-Tracking Technology

The principle of offset-tracking technology is to calculate the cross-correlation of the two time phases with a certain window size so as to obtain the sum of the offset caused by satellite orbit and surface deformation [37,38]. Then, according to the orbit data of the satellite, the offset caused by the satellite orbit is subtracted to obtain the deformation caused by the surface deformation. According to the information used in the cross-correlation calculation, offset-tracking technology can be divided into two implementations: intensity tracking and coherence tracking [39,40]. Because the intensity tracking method can overcome the phenomenon of decoherence, this algorithm is generally used for offset tracking. OT is mostly used in studies of large gradient deformation, and the study area experienced heavy rainfall in 2017 with a once-in-20-year event, with many areas deforming significantly; thus, using this method gives relatively reliable results.

The data processing flow is shown as follows (Figure 4).

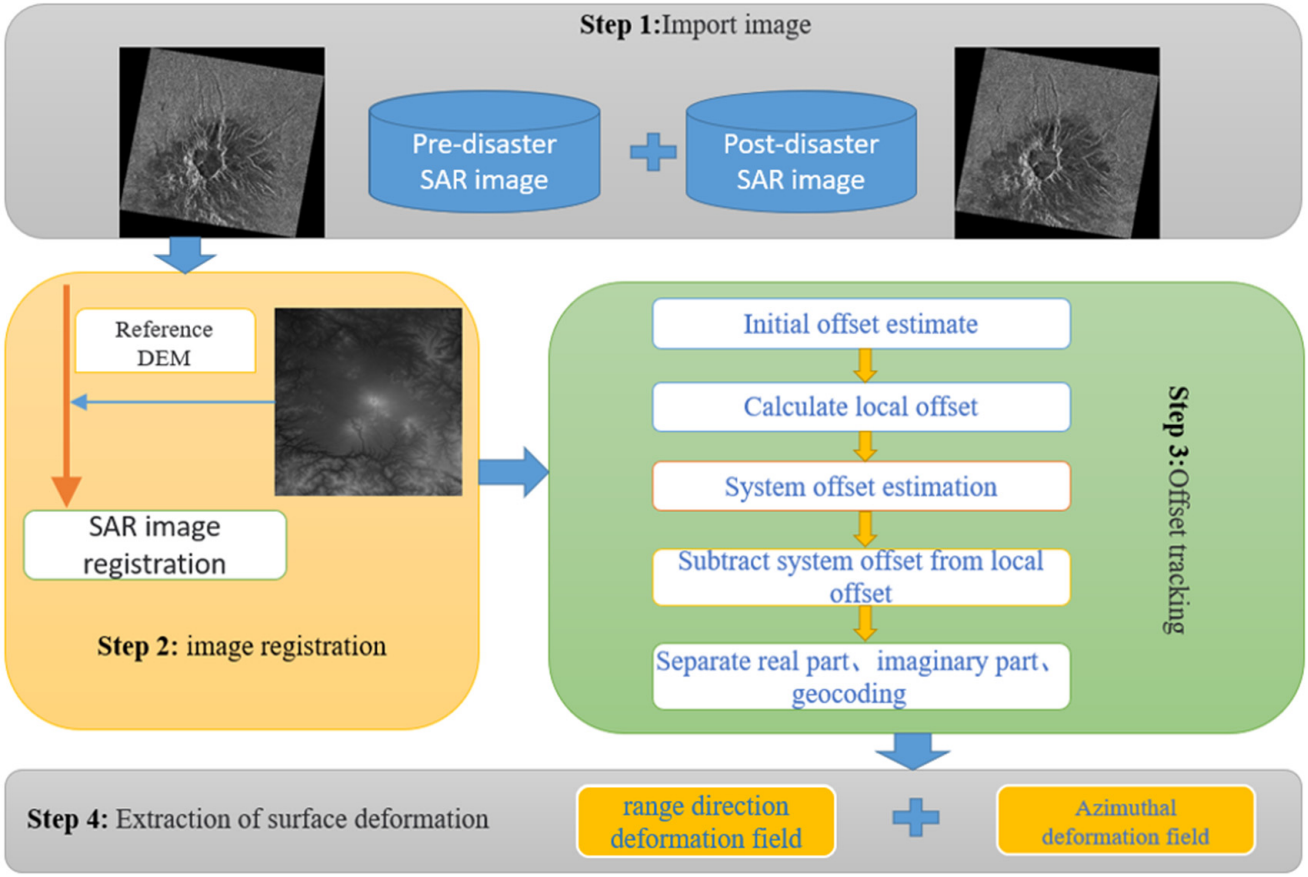

Figure 4. Flowchart of offset tracking data processing.

1. The SAR images of two time phases before and after the change are selected. According to the orbit parameter file during the satellite imaging, the offset of the SAR image caused by orbit error is calculated, and the image is roughly registered;
2. Accurate registration of two SAR images using the local window method to obtain a certain number of corresponding points from the two images, and then using the least squares polynomial fitting method to fit the mapping relationship between the two images. The registration of this step is crucial for the subsequent steps;
3. Using the intensity tracking method [41], we track the offset of the image to obtain the local offset;
4. The offset caused by the orbit is removed from the local offset obtained in the previous step, and the joint interferometry and offset tracking of the surface are obtained to extract the large gradient surface deformation offset. The range and azimuth deformation fields are separated from the offset, and the range and azimuth offset maps are geocoded and converted to the geographic coordinate system.

3.4. Differential Interferometry Synthetic Aperture Radar (D-InSAR) Technique

According to the interferometric mode, the D-InSAR technique can be divided into two-track, three-track and four-track differential interferometry, among which the two-track D-InSAR technique is the most widely used. The basic idea is to conjugate and multiply the SAR images before and after deformation, and then differential interferometric stripe maps are generated with DEM data to achieve the purpose of removing topography, i.e., weakening interference information, so as to obtain the topographic changes of ground targets in the study area [42–47].

In this paper, we use SARscape for differential interferometric radar (D-InSAR) processing, which consists of seven steps: data focusing, baseline estimation, interferogram generation, adaptive filtering and coherence generation, phase de-entanglement, track re-

finement and re-deplatforming and deformation conversion. In addition, there are several modules containing different operation steps. For example, in the interferogram generation, the interferometric data pair alignment and multi-view processing are included, and then the interferogram is generated after the processing, and the generated interferogram is based on the reference DEM image after the de-leveling of the interferometric image.

D-InSAR is prone to producing low frequency images when large-scale deformation occurs, so we simply use the method as a complement to OT, i.e., to verify OT where slow deformation can yield reliably deformed regions.

3.5. Remote Sensing Data

The SAR images used are collected by Sentinel-1, an earth observation satellite launched by the European Space Agency, which is equipped with a C-band SAR sensor. Sentinel-1 data can be registered and downloaded on the Sentinel Scientific Data Hub website at http://scihub.copernicus.eu/dhus (accessed on 3 May 2017). Details are shown in (Table 3). The acquisition mode of the image is IW, and the data format is SLC. The selection of 2017 Sentinel-1 data is due to the occurrence of debris flow in 8 gullies this year, of which No. 1 and No. 2 gullies occurred twice, and a large area of collapse and landslide occurred at Longmen Peak. Taking this as the source data can help us to obtain better offset-tracking demonstration results, and, using Google Maps as the base map to distinguish the deformation location, the resolution is 2.5 m. Considering the large topographic relief in this area, a 30 m resolution digital elevation model (SRTM1 Arc-Second Global, shuttle radar topography mission) (https://earthexplorer.usgs.gov/ (accessed on 3 May 2017)) is introduced to assist image registration and final terrain correction.

Table 3. Sentinel-1 data and imaging parameters.

Serial Number	Image Acquisition Time	Absolute Orbits	Relative Orbit	Azimuth Angle (°)	Incidence Angle (°)	Satellite Geometry
01	2017/01/01	3660	134	193	41	descending
8910310002	2017/03/07	4608	32	193	34	descending
03	2017/05/30	5833	32	193	34	descending
04	2017/09/03	3354	32	193	34	descending
05	2017/11/26	4058	32	193	34	descending
06	2017/12/20	3660	32	193	34	descending
07	2017/12/27	8910	134	193	41	descending
08	2018/03/03	9858	32	193	34	descending

4. Result

4.1. Debris Flow Solid out Volume

In order to explore the physical sources and the extent of each debris flow trench in the study area, we conducted a one-month geological survey of the study area in September 2018. According to the field investigation results, we have ascertained the provenance and reserves of the formation area, and, according to the type of provenance, they can be divided into three types: collapse-slip accumulation source, slope erosion source and channel accumulation source (Table 4).

On 2 July 2017, debris flow occurred in eight debris flow gullies in the northern scenic spot. According to the formula given in 3.2, the solid outflow of each debris flow ditch was calculated. The calculation results for each parameter are shown in Table 5. Among the debris flows caused by the rainfall, the No. 2 ditch has the most solid outflow, reaching 0.34×10^4 m^3, and the No. 7 ditch has the least solid outflow, reaching 0.01×10^4 m^3. Through regression analysis, we found that there is a strong power function correlation between the loose material reserves (V_m) of the debris flow ditch and the single debris flow solid source discharge (Q_H) (Figure 5): $V_m = 0.0089 Q_H^{1.3156}$, $R^2 = 0.9935$. The amount of debris flow solid material increased with the increase of loose material reserves; that is, when the study area has more material source reserves, the greater the risk of debris flow.

Table 4. Statistical table of sources of debris flow ditches in the Changbai Mountain North Scenic Area.

Ditch Number	Landslide Accumulation Source (10^4 m^3)	Slope Erosion Source (10^4 m^3)	Ditch Accumulation Source (10^4 m^3)	Total (10^4 m^3)
No. 1 ditch	6.13	2.91	1.96	11
No. 2 ditch	7.65	3.4	4.55	15.6
No. 3 ditch	1.7	1.8	0.19	3.69
No. 4 ditch	2.95	0.74	1.38	5.07
No. 5 ditch	0.59	1.71	0	2.3
No. 6 ditch	0.6	1.6	0	2.2
No. 7 ditch	0.62	1.28	0	1.9
No. 8 ditch	1.8	0.34	0.22	2.36
total	21.45	12.07	8.3	44.12

Table 5. Solid discharge of each debris flow ditch.

Ditch Number	Total Amount of Debris Flow (10^4 m^3)	Debris Flow Severity (t/m^3)	Water Severity (t/m^3)	Solid Material Weight of Debris Flow (t/m^3)	Solid Material Discharge of Debris Flow (10^4 m^3)
No. 1 ditch	0.49	1.70	1	2.50	0.23
No. 2 ditch	0.70	1.72	1	2.50	0.34
No. 3 ditch	0.06	1.48	1	2.50	0.02
No. 4 ditch	0.09	1.77	1	2.50	0.04
No. 5 ditch	0.07	1.48	1	2.50	0.03
No. 6 ditch	0.05	1.53	1	2.50	0.02
No. 7 ditch	0.04	1.49	1	2.50	0.01
No. 8 ditch	0.09	1.57	1	2.50	0.03

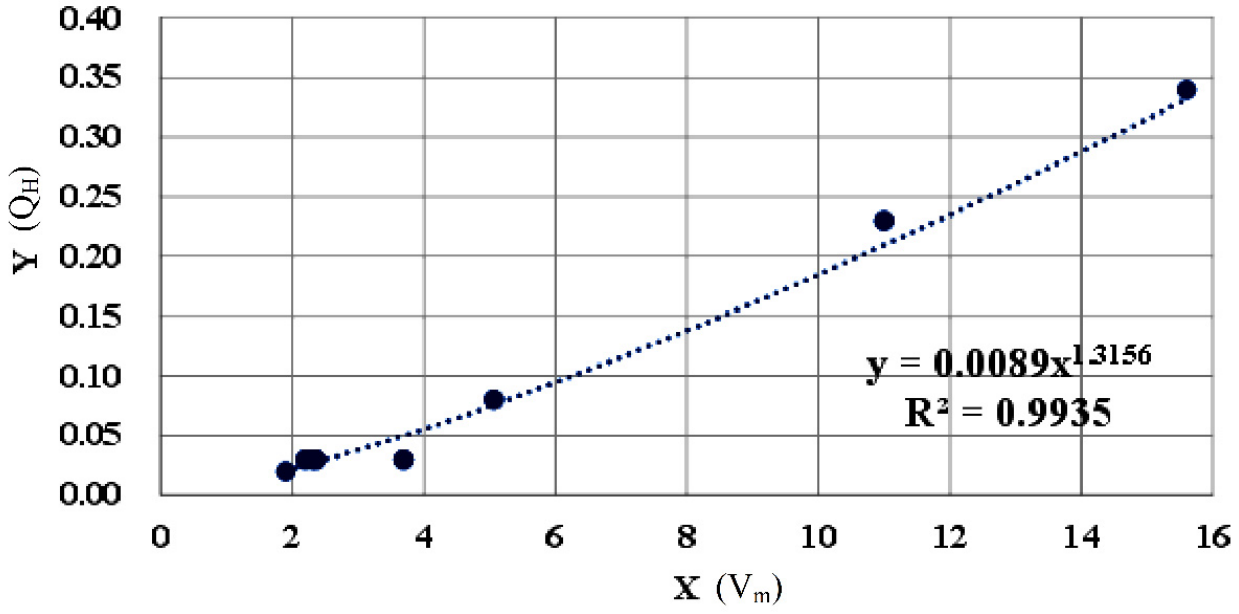

Figure 5. Relationship between source reserves and solid discharge of debris flow in the study area.

4.2. Offset Tracking Processing Results

The cross-correlation window size was adjusted and set to 16 × 16; the window size coherence was 8 × 8, and the coherence coefficient was 0.3. The Sentinel-1 data of the study area on 1 January 2017 and 27 December 2017 were processed by offset tracking to obtain the range direction (along the satellite line of sight) and azimuth direction (satellite orbit direction) of the study area during this time period. The results of displacement deformation in the direction of travel are shown in Figure 6. It can be seen from the figure that the range deformation in the study area in 2017 was very small, mainly in the azimuth direction. In order to ascertain the variation of provenance in the study area in each season, we use the six-scene Sentinel-1 data (since the end of each season is close to the beginning

of another season, the same scene data are used) to study the surface deformation of the area in each season which has been monitored. By using the formula $\Delta x = \sqrt{\Delta l^2 + \Delta p^2}$, the deformation of azimuth and distance is transformed into total displacement (Δl, Δp are the range offset and azimuth offset) (Figure 7). From the graph, it can be observed that the deformation in the study area is at its maximum during summer, with a maximum positive deformation of 130 mm/qr and a maximum negative deformation of 138 mm/qr. It should be noted that varying amounts of deformation are observed near each debris flow channel, which is due to the presence of large areas of slope debris near these channels. However, based on field surveys, it was found that these solid debris do not participate in the debris flow process; hence, they were not considered (Figure 8). Moreover, due to the growth of vegetation during summer, densely vegetated areas may cause signal obstruction or reflection, leading to increased precision error in offset tracking. The growth and change in vegetation can also cause changes in surface height, affecting the accuracy of offset tracking. Another point to consider is that the deposition areas of each debris flow channel are close to Erdaobai river; as the peak flow of Erdaobai river during the rainy season reaches 140 m^3/s, the debris flow materials are more likely to be carried away by the main river flow. Therefore, some deposition areas of debris flow may not exhibit positive deformation during summer, and channels numbered 4, 6 and 7 may even be affected by floods, resulting in negative deformation. In the circulation area of debris flow gully, due to the entrainment of debris flow, the deformation is basically negative in the figure, while the deformation amount in the formation area of the debris flow channel also varies depending on the size of the landslide supply from upstream. Therefore, the OT result alone is insufficient to determine the physical characteristics of the debris flow area and must be combined with field surveys or interpretations of remote sensing images to obtain more accurate results. However, analyzing the deformation amount in different areas based on OT results can help to determine the trend of debris flow development.

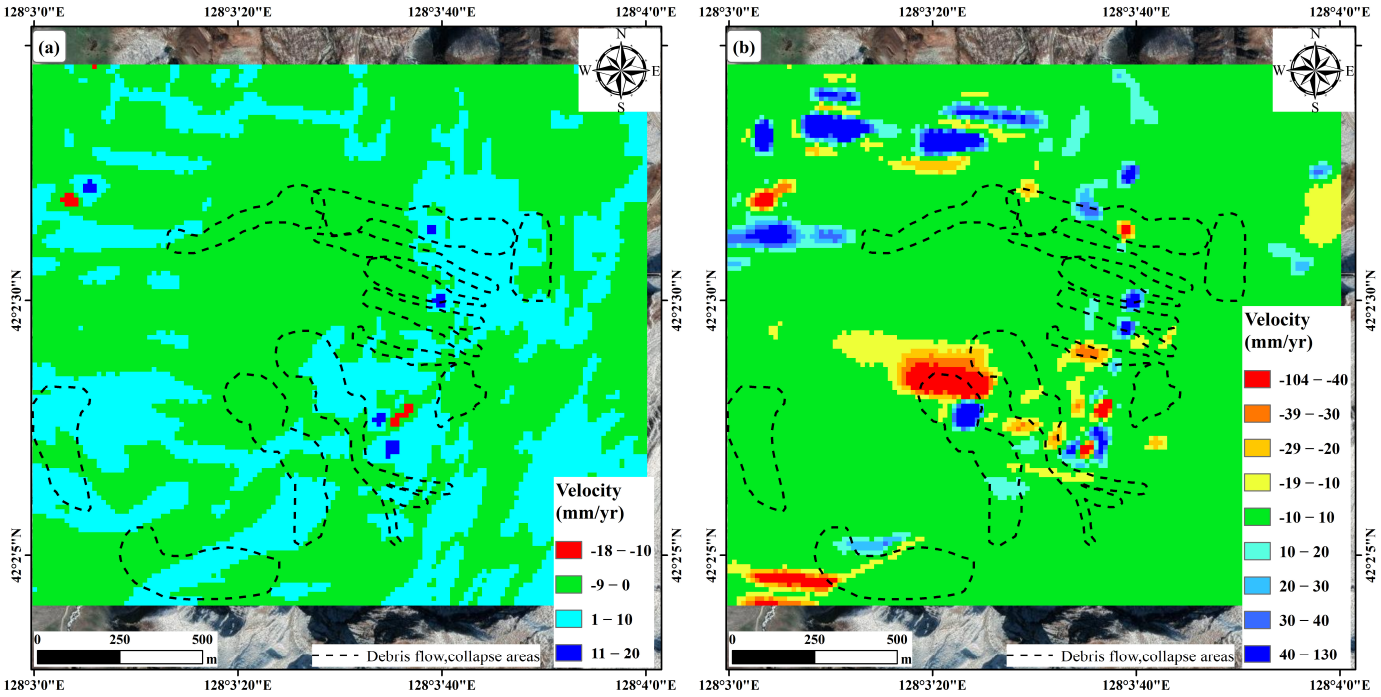

Figure 6. Results of surface deformation offset tracking in the study area (2017/01/01–2017/12/27). (**a**) Range direction; (**b**) azimuth direction.

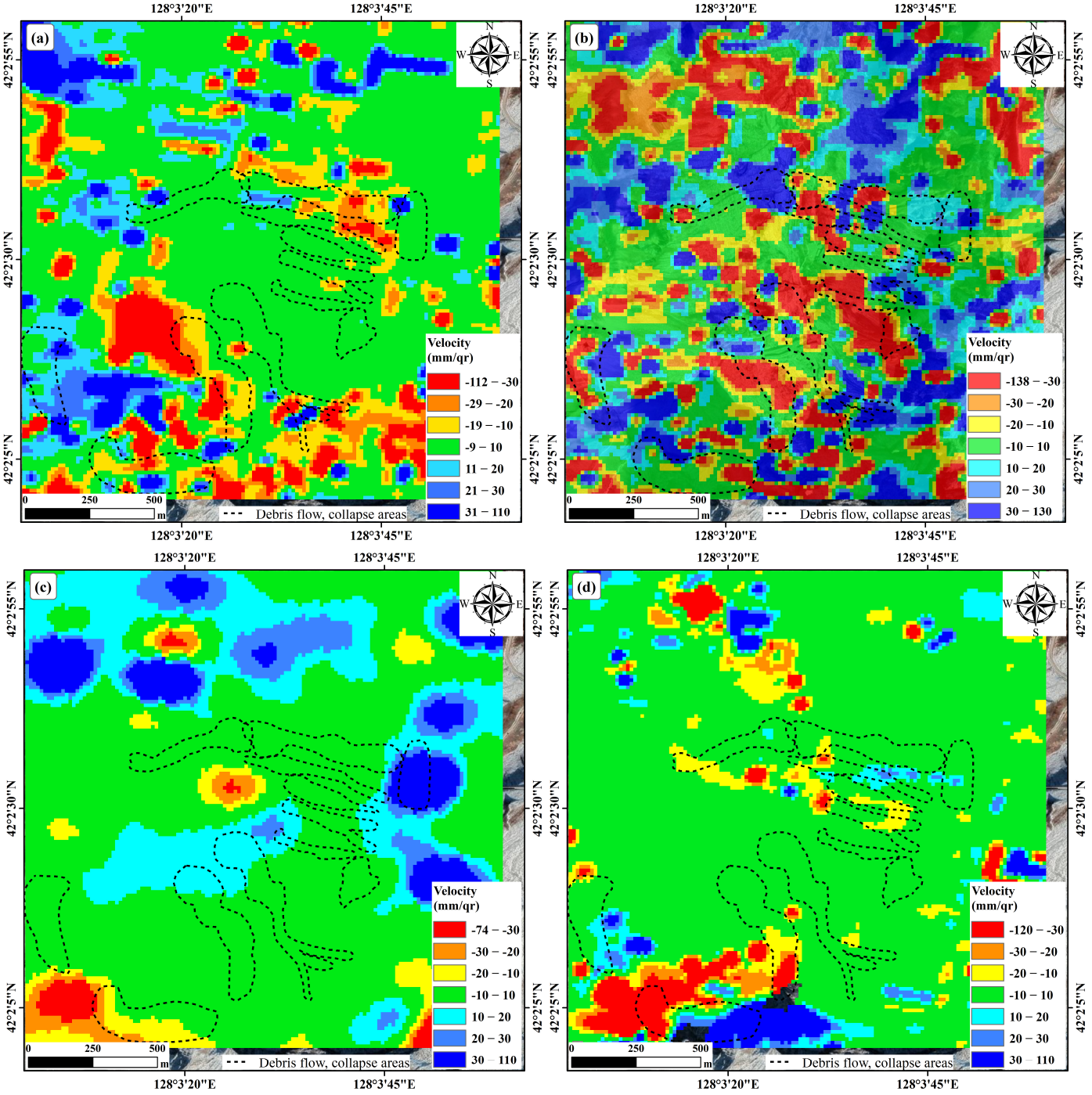

Figure 7. OT processing results of surface deformation in the study area in 2017. (**a**) Spring deformation (2017/03/07–2017/05/30); (**b**) summer deformation (2017/05/30–2017/09/03); (**c**) autumn deformation (2017/09/03–2017/11/26); (**d**) winter deformation (2017/11/26–2018/03/03).

Figure 8. The slope debris near the debris flow channel and the vegetation that begins to grow in summer.

4.3. D-InSAR Processing Results

Following the surface deformation analysis of the study area using the offset-tracking technique, we monitored the deformation of the study area by seasonal variation sing D-InSAR. The coherence threshold is 0.3, and the results are shown in the Figure 9. It can be seen from the figure that for each season, there is a certain range of blocky coherence loss areas (blank areas in the figure), where the maximum positive deformation that can be represented in the figure for each season is 78 mm, and the maximum negative deformation is 80 mm. Although D-InSAR does not provide a complete picture of deformation at every location in the study area, the ability to detect deformation in areas of slow deformation (e.g., autumn and winter) is unmatched by offset tracking. For example, the OT results for the study area in autumn and winter only reveal a trace of deformation but not the location, whereas D-InSAR demonstrates complete performance. However, D-InSAR results are not completely reliable and need to be used in conjunction with OT to obtain better analysis; for example, in Figure 9a, the low-frequency image, possibly due to Unwrap error, shows a south-to-north transition in the image, which is clearly not reliable.

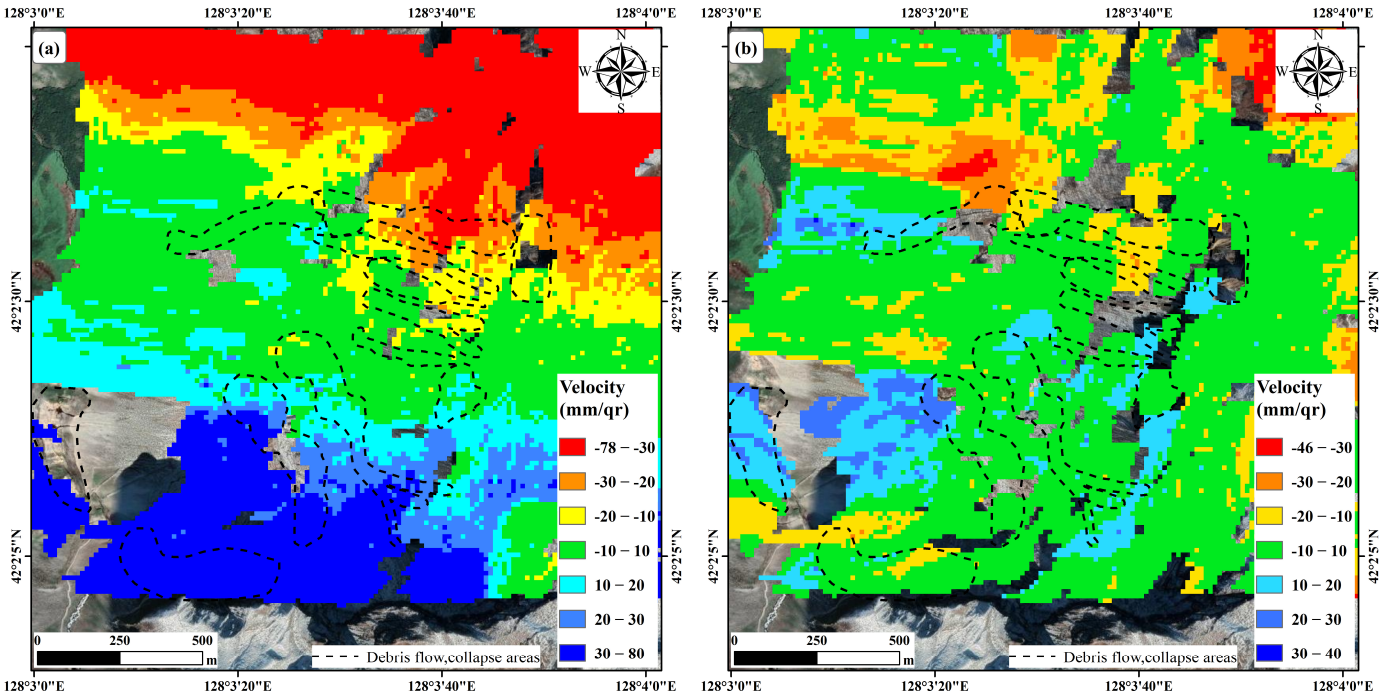

Figure 9. *Cont.*

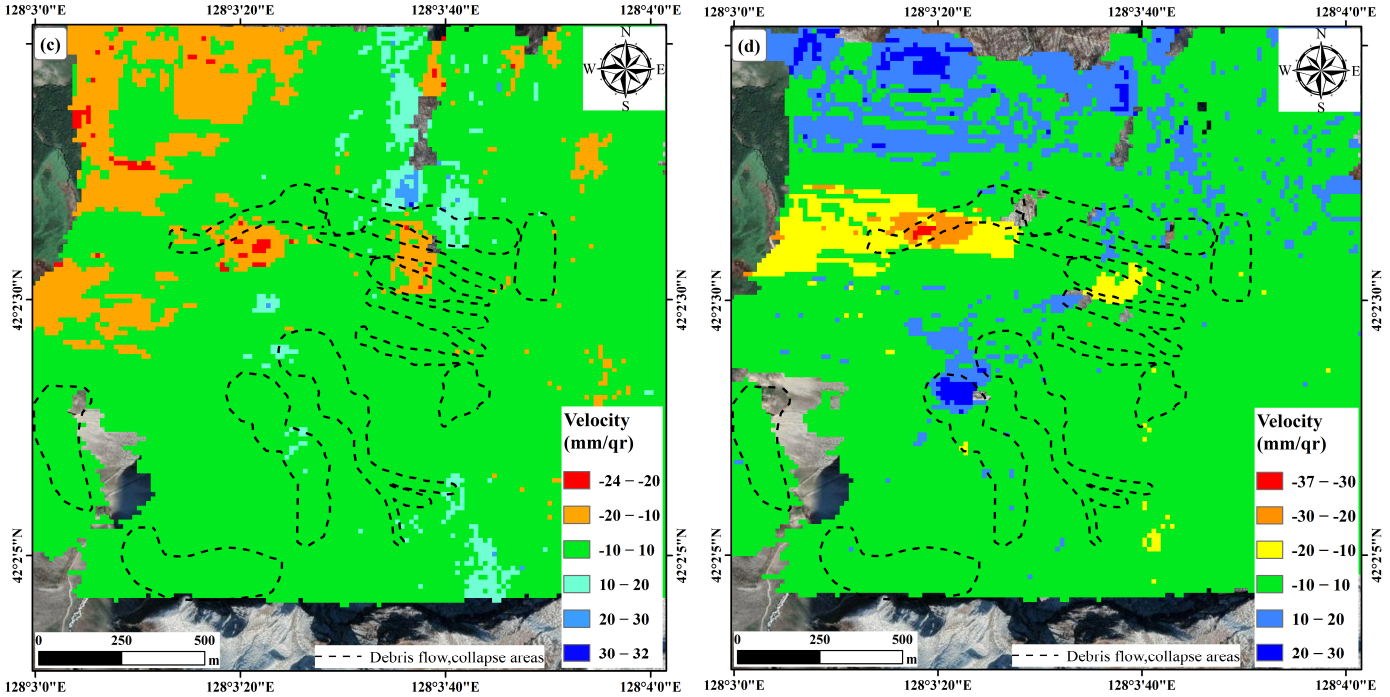

Figure 9. D-InSAR processing results of surface deformation in the study area in 2017. (**a**) Spring deformation (2017/03/07–2017/05/30); (**b**) summer deformation (2017/05/30–2017/09/03); (**c**) autumn deformation (2017/09/03–2017/11/26); (**d**) winter deformation (2017/11/26–2018/03/03).

4.4. Debris Flow Danger Zone in Scenic Area

According to the surface deformation monitoring results in the study area, combined with remote sensing images and field surveys, six debris flow risk areas in the scenic area of the study area were delineated, as shown in (Figure 10). Red is the monitored dangerous area determined according to the debris flow accumulation area, and yellow is the debris flow dangerous area determined by the field investigation. We can see that the monitoring results are very close to the field investigation results, which proves that OT has applicability in debris flow disaster prevention and mitigation. Among them, (a) is the No. 1 debris flow ditch danger zone, which includes the waterfall viewing platform, and the preliminary statistics threat number is 30,000 people; (b) is the No. 2 ditch debris flow dangerous area, which includes the scenic area's downstream trestle waterfall viewing platform, and the preliminary statistics threat number is 40,000 people; (c) and (h–f) are, respectively, No. 3 and No. 6–8 debris flow ditch dangerous areas, including the Julong hot spring scenic area and ditch mouth scenic area infrastructure, and the preliminary statistics threat number is 20,000 people; (d) is the No. 4 ditch debris flow danger zone, which includes the scenic parking lot and highway, and the preliminary statistics threat number is 40,000 people; (e) is the No. 5 ditch debris flow danger zone, for which there is no direct threat; (i) is the Longmen peak collapse landslide danger zone. It can be seen from the scope of the danger zone delineated in the figure that the danger range of No. 1 and No. 2 ditches is much larger than those of other debris flow ditches, which is positively correlated with the amount of solid outflow calculated by us. In the No. 2 ditch, solids flowed out of the accumulation area near the Erdaobai River, but because the debris flow outbreak season is the rainy season, the Erdaobai River peak flow of 140 m^3/s debris flow material will flow away with the main river water, so it will not cause a blocking the Erdaobai River's main channel.

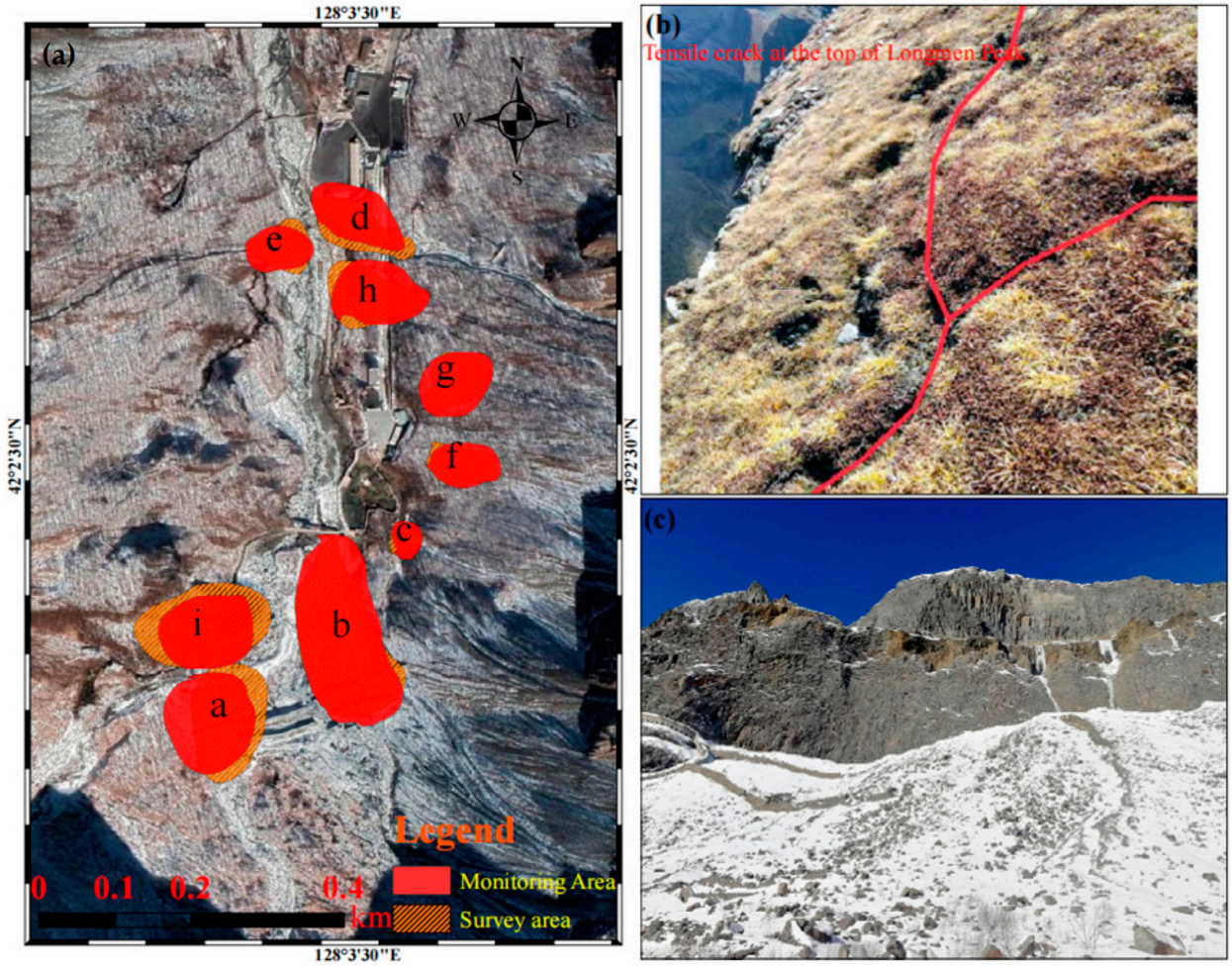

Figure 10. (**a**) North scenic dangerous area; (**b**) Longmen peak dangerous rock belt top; (**c**) Longmen peak dangerous rock belt side.

5. Discussion

5.1. Error Analysis

The root mean square error (RMSE) of D-InSAR and OT is an error metric used to evaluate the results of surface deformation measurements, and it is usually used to evaluate the accuracy and reliability of D-InSAR and OT algorithms. The minimum accuracy requirement is satisfied when the result is less than 100, and the smaller it is, the higher the reliability of the result. The RMSE values can be accessed in the report of the result file after the processing is completed. The RMSE values of offset tracking are 12.9, 95.8, 5.7 and 13.6, and the RMSE values of D-InSAR are 135, 217, 35.8 and 45.5, respectively. The RMSE values of D-InSAR are higher in both spring and summer, while OT meets the minimum value of reliability. Therefore, the combination of these two methods has some reliability when used to determine the changes of the source within the mudflow range that we have investigated in the field and interpreted by remote sensing. However, both methods are subject to certain limitations, leading to errors in accuracy. These include the height change due to the growth of vegetation in summer, which we mentioned in the previous section, and which will affect the monitoring accuracy, and the obscuring effect of terrain and vegetation may also lead to the unfolding error of D-InSAR. The radar reflection signal is affected by terrain and vegetation, and these effects will lead to different propagation times and paths of the signal between different areas, thus causing phase differences in unfolding [48]. Thus, phase differences occur and cause unfolding errors. Therefore, it is difficult and unreliable for researchers to rely on this method to determine the extent of the mudslide area, which

requires a combination of field survey and high-precision remote sensing images. There is also the fact that the time baseline we used in the paper is too long for to be used to obtain the variation of the source under different seasons, which will increase the ranging error in the data and thus reduce the positioning accuracy. In addition, a long time baseline also means that the signal is reflected or interfered with several times, which will further increase the accuracy error, and improving accuracy and reliability requires the selection of appropriate techniques and algorithms for data processing and correction [49].

For OT, although it can show a good performance in large gradient deformation, large gradient deformation also increases the difficulty of image alignment during processing, and incomplete alignment can have a large impact on accuracy, and the lower root mean square error in the summer period may be related to incomplete alignment. Preprocessing is needed to improve the stability and accuracy of the whole matching process. Jia H. proposed an improved uniform sample-based adaptive noncoherent scattering offset-tracking algorithm, which improves the speed and accuracy of co-alignment.

In addition to showing poor results in large gradient deformation monitoring, D-InSAR is not and will not be completely reliable for deformation monitoring in slowly deforming areas. For example, in this study on the amount of spring variation of mudflow sources using D-InSAR, the resultant images show a low frequency image transitioning from south to north during the unfolding process. In D-InSAR processing, low-frequency images caused by unfolding errors are generated due to the limitation of interferometric stripes, and the unfolding errors are usually caused by two factors: the large-scale deformation of the Earth's surface and the inhomogeneity of the propagation medium. The study area is covered with ice and snow in winter, and the shape of the medium changes when the ice melts in spring, resulting in possible changes in the path of the light, which affects the accuracy and reliability of phase untwisting. In addition, the melting of snow and ice will produce a large amount of water vapor, which will interfere with the propagation of light, and which will also cause some difficulties for phase decoupling. Therefore, for the ice-covered areas, the introduction of information from other data sources as constraints can be considered in the calculation process, or the D-InSAR method with multiple time phases can be used so as to reduce the influence of the unfolding error and improve the accuracy and reliability of deformation monitoring.

5.2. Offset Tracking Processing Results

In this study, we analyzed the relationship between the amount of debris flow solid discharge and the source reserves, but in fact, the amount of debris flow solid discharge is affected by many characteristic parameters [50]. By studying the relationship between the amount of loose source in the basin, the relative height difference of the basin and the amount of debris flow discharge, the prediction research is carried out by Bovis [51]. By analyzing the characteristics of the debris flow in the Wenchuan earthquake area, the mathematical relationship between the debris flow discharge and the loose material source is obtained by Ma [52]. An American scholar, Gartner, combined the three factors of debris flow basin area [53], landslide source area and cumulative rainfall to count the debris flow ditch in Corolla, analyzed the relationship between debris flow discharge and the three factors, and established the prediction model of debris flow discharge. The type and influence degree of these parameters can provide some data support for the prevention and control project of debris flow in the study area, suggesting that the prevention and control project can maximize the effect of disaster prevention and mitigation [54–56].

We analyzed the correlation and significance between debris flow solid outflow (Q_H) and ditch length (GL), ditch area (AOC), relative elevation difference (RED), mean longitudinal slope (MLS), source reserve (V_m), collapse accumulation source (LAS), slope erosion source (SES) and ditch accumulation source (GAS). Here, we also divide the provenance into slump deposit source, slope erosion source and ditch deposit source. Because of different debris flow gullies due to the different ditch forms, rainfall conditions and the distribution of material sources in the ditch, the main types of material sources involved

in debris flow will be different. The correlation and significance analysis results pertaining to these characteristic parameters and the number of solid debris flows are shown in Figures 11 and 12.

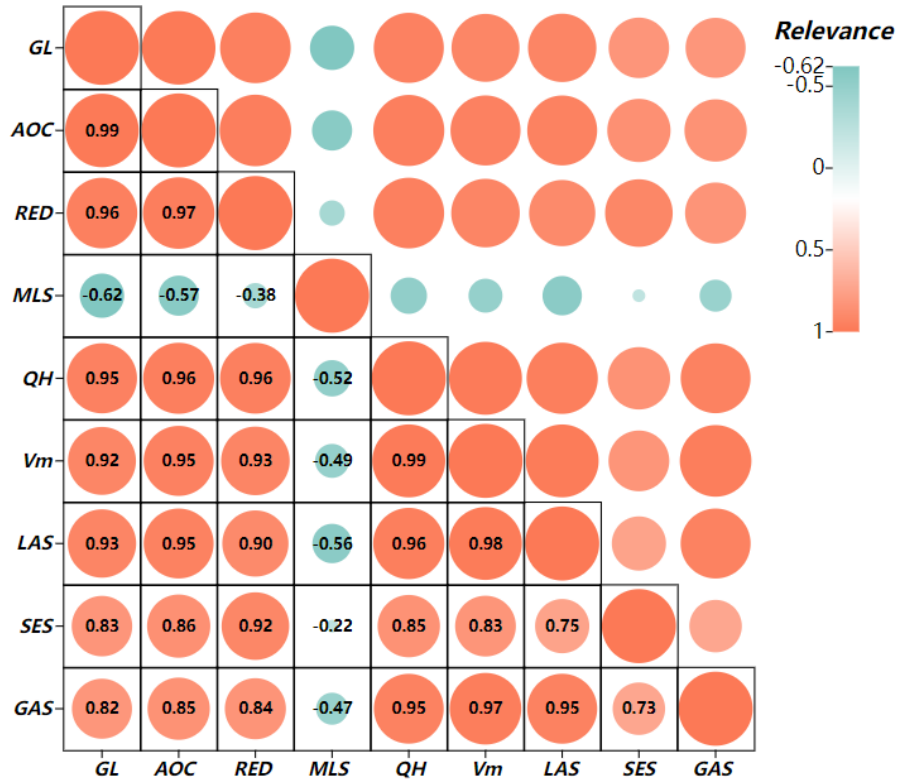

Figure 11. Correlation analysis results.

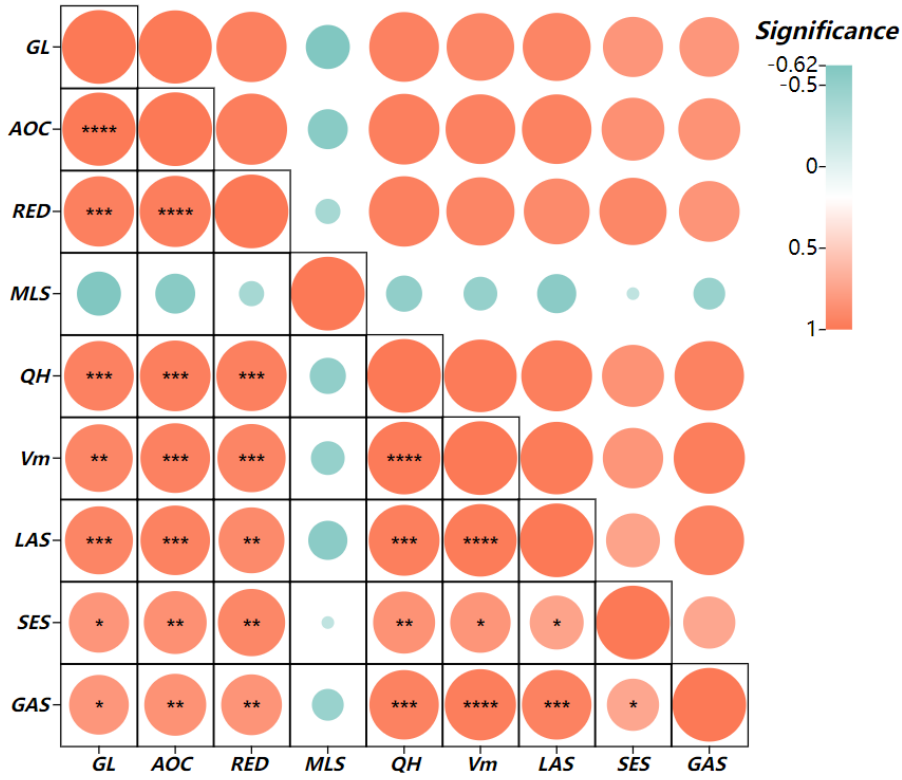

Figure 12. Significance analysis results. * expressed $p < 0.05$, ** expressed $p < 0.01$, *** expressed $p < 0.001$, **** expressed $p < 0.0001$.

According to the analysis results, except that the p value of the average longitudinal slope is negative, there is a strong positive correlation between the amount of debris flow and other parameters. It shows that these characteristic parameters have a strong influence on the amount of solid debris flow in this study area. There is a strong correlation between the three types of material sources of landslide accumulation, slope erosion, ditch accumulation and the amount of solid debris flow. Among them, the sources of landslide accumulation and ditch accumulation are up to 0.98 and 0.97, respectively, indicating that these two types of sources participate in debris flow activities. In the future monitoring of disaster prevention and mitigation, we should pay special attention to the changes of these two parameters.

6. Conclusions

Monitoring the change of provenance in the study area is an effective means of debris flow early warning and prevention. In this paper, we combine field investigation, remote sensing imaging and offset-tracking technology to monitor the deformation of solids in the study area. The conclusions are as follows:

1. According to the comparison between the solid washout from the mudflow we calculated, and the loose material source reserves obtained from the survey, the solid washout from a single mudflow is much smaller than the material source reserves. Combined with the analysis of the OT results, even after the occurrence of mudflow, the formation area of multiple mudflows will be recharged by material sources due to the collapse landslide above, and the recharge will be even greater than the consumption. Therefore, the frequency of mudflow outbreaks in the study area may be more frequent in the summer when heavy rainfall is encountered for a long time in the future;
2. Although OT is widely used for large gradient deformation, and although we can use it to determine the physical source variability of mudflows in the study area, for different study purposes, the OT results are not completely reliable. For example, as we mentioned in 4.2, we cannot use the OT results alone to delineate the extent of mudflows, and its results are affected by various factors such as vegetation, rainfall and weather. Therefore, in the study of mudslides, it is necessary to combine field surveys or remote sensing images to delineate the extent of mudslides;
3. Combined with remote sensing images, field survey and offset tracking results delineated the mudslide danger zone in the scenic area of the study area. Due to the huge number of visitors in the scenic area—according to our preliminary statistics, the total number of people threatened reached 130,000—it is necessary to do a good job of disaster prevention and mitigation and protection work in the danger zone, especially at the danger zone of the collapse of Longmen Peak, where there have been many incidents of falling rocks injuring people;
4. We have used D-InSAR for deformation monitoring after deformation monitoring using offset tracking, a method which, although subject to many factors when deforming large gradients, can be used as a complement to offset-tracking techniques. D-InSAR can operate effectively in areas with slow deformation, and it can be used in combination with offset tracking to obtain more highly accurate surface shape information. We see an opportunity here to develop a hybrid velocity product combining D-InSAR and offset tracking results in the areas where one method or the other- or both-perform best, as suggested by Joughin [54] and Liu [55], in order to obtain more reliable deformation monitoring results;
5. In snow and ice covered areas, the effect of snow and ice melting may increase the error of phase untwisting, which, in turn, leads to low-frequency images. Therefore, the monitoring accuracy and results of D-InSAR will be greatly affected during the ice and snow melting in spring, and even if the deformation is small, the monitoring results cannot be fully trusted and need to be used in combination with other methods;

6. We learned from analyzing the relationship between various parameters in the watershed, as well as the quantity of washed out debris flow solids, that the source of avalanche-slip accumulation and the source of channel accumulation have a high correlation with the amount of debris flow solids washed out, and we should consider increasing the weight of these two factors when predicting the development trend of debris flow.

Author Contributions: Conceptualization, J.Y.; Data curation, J.Y. and Y.Z.; Formal analysis, J.Y. and Y.C.; Methodology, J.Y. and Y.C.; Writing—Original draft, J.Y.; Funding acquisition, J.Z. and Z.Z.; Writing—Review and Editing, Z.Z. All authors have read and agreed to the published version of the manuscript.

Funding: This study was funded by the major scientific and technological research project of Jilin 404 Province (20220203185SF) and the soft science research project of Jilin Provincial Department of 405 Natural Resources (120200073).

Institutional Review Board Statement: Not applicable.

Informed Consent Statement: Not applicable.

Data Availability Statement: The codes and data for this article are freely available at http://scihub.copernicus.eu/dhus (accessed on 3 May 2017), https://earthexplorer.usgs.gov/ (accessed on 3 May 2017).

Conflicts of Interest: The authors declare no conflict of interest.

References

1. Rickenmann, D.; Zimmermann, M. The 1987 debris flows in Switzerland: Documentation and analysis. *Geomorphology* **1993**, *8*, 175–189. [CrossRef]
2. Costa, J. Physical geomorphology of debris flows. In *Developments and Applications of Geomorphology*; Springer: Berlin/Heidelberg, Germany, 1984; pp. 268–317.
3. Hungr, O.; Evans, S.G.; Bovis, M.J.; Hutchinson, J.N. A review of the classi fication of landslides of the flow type. *Phys. Geomorphol. Debrisflows* **2001**, *7*, 221–238.
4. Hungr, O.; Leroueil, S.; Picarelli, L. The Varnes classification of landslide types. *Landslides* **2014**, *11*, 167–194. [CrossRef]
5. Iverson, R.M. The physics of debris flows. *Rev. Geophys.* **1997**, *35*, 245–296. [CrossRef]
6. Innes, J.L. Debris flows. *Prog. Phys. Geogr. Earth Environ.* **1983**, *7*, 469–501. [CrossRef]
7. Cesca, M.; D'Agostino, V. Comparison between FLO-2D and RAMMS in debrisflow modelling: A case study in the Dolomites. *WIT Trans. Eng.* **2008**, *60*, 197–206.
8. De Haas, T.; Braat, L.; Leuven, J.R.F.W.; Lokhorst, I.R. Kleinhans MGEffects of debrisflow composition on runout, depositional mechanisms, and deposit morphology in laboratory experiments. *Geophys. Res. Earth Surf.* **2015**, *120*, 1949–1972. [CrossRef]
9. Ji, F.; Dai, Z.; Li, R. A multivariate statistical method for susceptibility analysis of debris flow in southwestern China. *Hazard. Earth Syst.* **2020**, *20*, 1321–1334. [CrossRef]
10. Viesca, R. Debris flow: Mechanics, prediction and countermeasures by Tamotsu Takahashi. *Pure Appl. Geophys.* **2008**, *165*, 995. [CrossRef]
11. Chen, H.X.; Zhang, L.M.; Chang, D.S.; Zhang, S. Mechanisms and runout characteristics of the rainfall-triggered debris fow in Xiaojiagou in Sichuan Province, China. *Nat. Hazard.* **2012**, *62*, 1037–1057. [CrossRef]
12. Simoni, A.; Mammoliti, M.; Graf, C. Performance of 2D debris fow simulation model RAMMS. Back-analysis of feld events in Italian Alps. *Annu. Int. Conf. Geol. Earth Sci.* **2012**, *20*, 1521–1534.
13. Breien, H.; De Blasio, F.V.; Elverhøi, A.; Høeg, K. Erosion and morphology of a debris flow caused by a glacial lake outburst flood, Western Norway. *J. Landslides* **2008**, *5*, 271–280. [CrossRef]
14. Bel, C.; Li'ebault, F.; Navratil, O.; Eckert, N.; Bellot, H.; Fontaine, F.; Laigle, D. Rainfall control of debris-flow triggering in the Real Torrent, Southern French Prealps. *Geomorphology* **2017**, *291*, 17–32. [CrossRef]
15. Dowling, C.A.; Santi, P.M. Debris flows and their toll on human life: A global analysis of debris-flow fatalities from 1950 to 2011. *Nat. Hazard.* **2014**, *71*, 203–227. [CrossRef]
16. Lee, S.G.; Winter, M.G. The effects of debris flow in the Republic of Korea and some issues for successful risk reduction. *Eng. Geol.* **2019**, *251*, 172–189. [CrossRef]
17. Pastorello, R.; D'Agostino, V.; Hürlimann, M. Debris flow triggering characterization through a comparative analysis among different mountain catchments. *Catena* **2020**, *186*, 104–348. [CrossRef]
18. Bernard, M.; Gregoretti, C. The use of rain gauge measurements and radar data for the model-based prediction of runoff-generated debris-flow occurrence in early warning systems. *Water Resour.* **2021**, *57*, e2020WR027893. [CrossRef]
19. Berti, M.; Bernard, M.; Gregoretti, C.; Simoni, A. Physical interpretation of rainfall thresholds for runoff-generated debris flows. *Geophys. Res. Earth Surf.* **2017**, *125*, e2019JF005513. [CrossRef]

20. Cao, C.; Zhang, W.; Chen, J.; Shan, B.; Song, S.; Zhan, J. Quantitative estimation of debris flow source materials by integrating multisource data: A case study. *Eng. Geol.* **2019**, *291*, 106–222.
21. Caine, N. The rainfall intensity-duration control of shallow landslides and debris flows. *Geogr. Ann. Ser.* **1980**, *62*, 23–27.
22. Dewitte, O.; Jasselette, J.C.; Cornet, Y.; Van Den Eeckhaut, M.; Collignon, A.; Poesen, J.; Demoulin, A. Tracking landslide displacements by multi-temporal DTMs: A combined aerial stereophotogrammetric and LIDAR approach in western Belgium. *Eng. Geol.* **2008**, *99*, 11–22. [CrossRef]
23. Stumpf, A.; Malet, J.-P.; Allemand, P.; Ulrich, P. Surface reconstruction and landslide displacement measurements with Pl'eiades satellite images. *Photogramm. Remote Sens.* **2004**, *95*, 1–12. [CrossRef]
24. Tseng, C.M.; Lin, C.W.; Stark, C.P.; Liu, J.K.; Fei, L.Y.; Hsieh, Y.C. Application of a multi-temporal, LiDAR-derived, digital terrain model in a landslide-volume estimation. *Earth Surf. Process. Landf.* **2013**, *38*, 1587–1601. [CrossRef]
25. Feng, G.; Hetland, E.A.; Ding, X.; Li, Z.; Zhang, L. Coseismic fault slip of the 2008 Mw 7.9 Wenchuan earthquake estimated from InSAR and GPS measurements. *Geophys. Res. Lett.* **2010**, *37*, 73–78. [CrossRef]
26. Strozzi, T.; Luckman, A.; Murray, T.; Wegmuller, U.; Werner, C.L. Glacier motion estimation using SAR offset-tracking proce dures. *J. IEEE Trans. Geosci. Remote Sens.* **2002**, *40*, 2384–2391. [CrossRef]
27. Elliott, J.L.; Freymueller, J.T.; Rabus, B. Coseismic deformation of the 2002 Denali fault earthquake: Contributions from synthetic aperture radar range offsets. *Geophys. Res. Solid Earth* **2007**, *112*, B6. [CrossRef]
28. Wang, T.; Jónsson, S. Improved SAR amplitude image offset measurements for deriving three-dimen sional coseismic displace-ments. *J. Sel. Top. Appl. Earth Obs. Remote Sens.* **2015**, *8*, 3271–3278. [CrossRef]
29. Schellenberger, T.; Dunse, T.; Kääb, A.; Kohler, J.; Reijmer, C. Surface speed and frontal ablation of kronebreen and kongsbreen, NW Svalbard, from SAR offset tracking. *Cryosphere* **2015**, *9*, 2339–2355. [CrossRef]
30. Wang, C.; Mao, X.; Wang, Q. Landslide displacement monitoring by a fully polarimetric SAR offset tracking method. *Remote Sens.* **2010**, *8*, 624. [CrossRef]
31. Fielding, E.J.; Lundgren, P.R.; Taymaz, T.; Yolsal-Çevikbilen, S.; Owen, S.E. Fault-slip source models for the 2011 M 7.1 van earthquake in Turkeyfrom SARinterferometry, pixel offset tracking, GPS, and seismic waveform analysis. *Seismol. Res.* **2013**, *84*, 579–593. [CrossRef]
32. Bai, C.; Wang, F.; Wang, L.; Xu, C.; Yue, X.; Yang, S.; Wang, P.; Bi, Y.; Wei, H. Dynamic Monitoring of Debris-Covered Glacier Surface Velocity and Ice Thickness of Mt.Tomur, Tian Shan, China. *Remote Sens.* **2023**, *15*, 150. [CrossRef]
33. Yang, H.; Tang, L.; Zhu, H.; Xu, A.; Li, B. A Concise Method for Calibrating the Offset of GPS Precise Satellite Orbit. *Remote Sens.* **2023**, *15*, 8. [CrossRef]
34. Yang, C.; Wei, C.; Ding, H.; Wei, Y.; Zhu, S.; Li, Z. Inversion of Glacier 3D Displacement from Sentinel-1 and Landsat 8 Images Based on Variance Component Estimation: A Case Study in Shishapangma Peak, Tibet, China. *Remote Sens.* **2023**, *15*, 4. [CrossRef]
35. Feng, J.; Qiu, Y.; Dong, C.; Ni, X.; Lin, W.; Teng, H.; Pan, A. Interannual Variabilities of the Southern Bay of Bengal Cold Pool Associated with the El Niño–Southern Oscillation. *Remote Sens.* **2023**, *14*, 6169. [CrossRef]
36. Zhu, Y.; Qiu, H.; Liu, Z.; Wang, J.; Yang, D.; Pei, Y.; Ma, S.; Du, C.; Sun, H.; Wang, L. Detecting Long-Term Deformation of a Loess Landslide from the Phase and Amplitude of Satellite SAR Images: A Retrospective Analysis for the Closure of a Tunnel Event. *Remote Sens.* **2021**, *13*, 4841. [CrossRef]
37. Gray, A.L.; Mattar, K.E.; Vachon, P.W.; Bindschadler, R.; Jezek, K.C.; Forster, R.; Crawford, J.P. InSAR results from the RADARSAT Antarctic Mapping Mission data: Estimation of glacier motion using a simple registration procedure. IGARSS'98. Sensing and Managing the Environment. 1998 IEEE International Geoscience and Remote Sensing. *Symp. Proc.* **1998**, *3*, 1638–1640. [CrossRef]
38. Yoo, J.C.; Han, T.H. Fast normalized cross-correlation. *Circuits Syst. Signal Process.* **2009**, *28*, 819–843. [CrossRef]
39. Jia, H.; Wang, Y.; Ge, D.; Deng, Y.; Wang, R. Improved offset tracking for predisaster deformation monitoring of the 2018 Jinsha River landslide (Tibet, China). *Remote Sens. Environ.* **2020**, *247*, 111899. [CrossRef]
40. Du, S.; Mallorqui, J.J.; Zhao, F. Patch-Like Reduction (PLR): A SAR Offset Tracking amplitude filter for defor mation monitoring. *Int. J. Appl. Earth Obs. Geoinf.* **2022**, *113*, 102976. [CrossRef]
41. Rott, H.; Stuefer, M.; Siegel, A.; Skvarca, P.; Eckstaller, A. Mass fluxes and dynamics of Moreno Glacier, Southern Patagonia Icefield. *Geophys. Res. Lett.* **1998**, *25*, 1407–1410. [CrossRef]
42. Chen, B.; Deng, K.; Fan, H.; Hao, M. Large-scale deformation monitoring in mining area by D-InSAR and 3D laser scanning technology integration. *Int. J. Min. Sci. Technol.* **2013**, *23*, 555–561. [CrossRef]
43. Mura, J.C.; Paradella, W.R.; Gama, F.F.; Silva, G.G.; Galo, M.; Camargo, P.O.; Silva, A.Q.; Silva, A. Monitoring of Non-Linear Ground Movement in an Open Pit Iron Mine Based on an Integration of Advanced DInSAR Techniques Using TerraSAR-X Data. *Remote Sens.* **2016**, *8*, 409. [CrossRef]
44. Debella-Gilo, M.; Kääb, A. Sub-pixel precision image matching for measuring surface displacements on mass movements using normalized cross-correlation. *Remote Sens. Environ.* **2011**, *115*, 130–142. [CrossRef]
45. Cheng, X.Q.; Ma, C.; Kang, J.R.; Zou, Y. Simulation and time series analysis of mining subsidence by integrating DInSAR and PIM technology. *J. China Univ. Min. Technol.* **2018**, *47*, 1141–1148.
46. Pawluszek-Filipiak, K.; Borkowski, A. Integration of DInSAR and SBAS Techniques to Determine Mining-Related Deformations Using Sentinel-1 Data: The Case Study of Rydułtowy Mine in Poland. *Remote Sens.* **2020**, *12*, 242. [CrossRef]
47. Xu, B.; Li, Z.; Zhu, Y.; Shi, J.; Feng, G. SAR Interferometric Baseline Refinement Based on Flat-Earth Phase without a Ground Control Point. *Remote Sens.* **2020**, *12*, 233. [CrossRef]

48. Zhao, X.; Zhou, D.; Fang, J. Satellite-based Studies on Large-Scale Vegetation Changes in China. *J. Integr. Plant Biol.* **2012**, *54*, 713–728. [CrossRef]
49. Mirmohammadian, F.; Asgari, J.; Verhagen, S.; Amiri-Simkooei, A. Multi-GNSS-Weighted Interpolated Tropospheric Delay to Improve Long-Baseline RTK Positioning. *Sensors* **2022**, *22*, 5570. [CrossRef]
50. D'Agostino, V.; Marchi, L. Debris flow magnitude in the eastern italian alps: Data collection and analysis. *J. Phys. Chem. Earth* **2001**, *26*, 657–663. [CrossRef]
51. Bovis, M.J.; Jakob, M. The role of debris supply conditions in predicting debris flow activity. *J. Earth Surf. Process. Landf.* **1999**, *24*, 1039–1054. [CrossRef]
52. Ma, C.; Hu, K.; Tian, M. Comparison of debris-flow volume and activity under different formation conditions. *Nat. Hazard.* **2013**, *67*, 261–273. [CrossRef]
53. Gartner, J.E.; Cannon, S.H.; Santi, P.M.; Dewolfe, V.G. Empirical models to predict the volumes of debris flows generated by recently burned basins in the western U.S. *Geomorphology* **2008**, *96*, 339–354. [CrossRef]
54. Chang, M.; Tang, C.; Van Asch, T.W.; Cai, F. Hazard assessment of debris flows in the Wenchuan earthquake-stricken area, South West China. *J. Landslides* **2017**, *14*, 1783–1792. [CrossRef]
55. Joughin, I. Ice-sheet velocity mapping: A combined interferometric and speckle-tracking approach. *Ann. Glaciol.* **2002**, *34*, 195–201. [CrossRef]
56. Liu, H.X.; Zhao, Z.Y.; Jezek, K.C. Synergistic fusion of interferometric and speckle-tracking methods for deriving surface velocity from interferometric SAR data. *IEEE Geosci. Remote Sens. Lett.* **2007**, *4*, 102–106. [CrossRef]